scientific reports

Check for updates

OPEN

Enhanced hydrogen evolution reaction activity through samarium-doped nickel phosphide (Ni_2P) electrocatalyst

Ali Shahroudi & Sajjad Habibzadeh✉

Hydrogen evolution reaction (HER) stands out among conventional hydrogen production processes by featuring excellent advantages. However, the uncompetitive production cost due to the low energy efficiency has hindered its development, necessitating the introduction of cost-effective electrocatalysts. In this study, we introduced samarium doping as a high-potential approach to improve the electrocatalytic properties of nickel phosphide (Ni_2P) for efficient HER. Samarium-doped Ni_2P was synthesized via a facile two-step vapor–solid reaction technique. Different physical and electrochemical analyses showed that samarium doping significantly improved pure Ni_2P characteristics, such as particle size, specific surface area, electrochemical hydrogen adsorption, intrinsic activity, electrochemical active surface area, and charge transfer ability in favor of HER. Namely, Ni_2P doped with 3%mol of samarium ($Sm_{0.03}Ni_2P$) with a Tafel slope of 67.8 mV/dec. and overpotential of 130.6 mV at a current density of 10 mA/cm^2 in 1.0 M KOH solution exhibited a notable performance, suggesting $Sm_{0.03}Ni_2P$ and samarium doping as a remarkable electrocatalyst and promising promoter for efficient HER process, respectively.

Keywords Electrocatalyst, Hydrogen evolution reaction, Nickel phosphide, Samarium, Doping

Ever-increasing world energy demand coupled with the distressing environmental issues posed by fossil fuel overconsumption has necessitated the urgent development of eco-friendly and sustainable energy sources[1]. In this regard, hydrogen has emerged as a promising alternative, considering its great energy density and clean combustion[2]. Among different hydrogen production methods, hydrogen evolution reaction (HER) excels in many aspects by producing high-purity hydrogen from abundant water resources at moderate conditions without undesired emissions[3]. However, the comparatively high HER-driven hydrogen cost due to poor energy efficiency has hindered its reasonable development and resulted in a small share of the hydrogen market, emphasizing the employment of active electrocatalysts[4]. Pt-group metals are known as the most active HER electrocatalysts. However, their scarcity and corresponding expensiveness have restricted their practical usage, highlighting the introduction of active yet affordable materials to enable the deserved development of HER[5].

Transition metal-based materials with low price, high abundance, and relatively easy preparation have shown notable performance in HER among which nickel phosphides, and particularly the Ni_2P crystalline phase by showing outstanding performance are regarded as future HER electrocatalysts[6]. Many researchers have considered the performance of pristine Ni_2P in HER[7–10]. However, despite promising activity, its performance has not yet been suited to real applications and requires further improvement. Thus, several approaches have been implemented, among which doping has shown significant potential. Thus far, transition metals or heteroatoms have mainly been studied as doping agents in HER electrocatalysis[11–20]. However, despite their excellent capability, rare-earth (RE) elements have not been well considered, and the HER electrocatalysis research area lacks sufficient studies on this area.

RE elements are 17 elements comprising scandium, yttrium, and 15 elements of the lanthanide series[21]. Unlike their title, RE elements are abundant in the Earth's crust[22]. However, since they have been widely dispersed over the Earth and are not concentrated in one location, they have historically been classified as *rare-earth* elements[23]. RE elements feature unique chemical, electronic, magnetic, and optical properties that have been used in a wide variety of applications. Their 4f orbitals allow various energy level transitions, making RE elements

Surface Reaction and Advanced Energy Materials Laboratory, Chemical Engineering Department, Amirkabir University of Technology (Tehran Polytechnic), Tehran, Iran. ✉email: sajjad.habibzadeh@mail.mcgill.ca

ideal for electrochemical applications such as supercapacitors, batteries, and electrocatalysis[24]. Namely, Engel-Brewer theories predict that doping RE-elements with empty or half-filled d-subshell orbitals, like cerium and samarium, into transition metals with available unpaired d-subshell orbitals, such as cobalt and nickel, can have a synergistic effect in favor of HER. This phenomenon has been illustrated by several theoretical computational studies. Moreover, multiple experimental researches from an empirical perspective have demonstrated the great potential of RE elements in HER[25–30].

In a pioneering study, Morse and Greene[31] explored the electrocatalytic activity of thirteen RE elements in HER and reported noteworthy performance for them. However, the scientific community shifted its focus towards combining RE elements with transition metals, considering their relatively greater capability[25,32]. In this regard, Miles[33] applied $LaNi_5$ alloy for the first time in HER, opening doors for researchers to investigate this alloy further[34]. Subsequently, various alloys consisting of transition metals combined with different RE elements were also considered[35–37], leading to the gradual development of research in this area. However, in the early studies, casting methods were predominantly employed to alloy transition metals and RE elements, which were deemed less desirable for several reasons. Therefore, researchers have increasingly used more advanced methods like doping to involve RE elements in recent years.

Gao et al.[26] studied cerium-doped CoP electrocatalyst in HER and demonstrated the notable effect of cerium doping in enhancing the performance of CoP. This finding was also reported in several similar studies[27–30]. Subsequently, researchers started to investigate the effect of cerium doping on nickel phosphides[38–40]. In a comprehensive work, our research group conducted a study on cerium-doped nickel phosphide (Ni_2P) using computational and experimental approaches, where the significant impact of cerium on the performance of Ni_2P was revealed[41]. The promising results of this study, along with the similar electronic structure of Lanthanides, motivated us to investigate further the effects of other RE elements to broaden the horizons in this field of research. Therefore, we focused on samarium doping in the present study to achieve efficient HER electrocatalysis.

This study introduces samarium as a novel promoter to enhance the electrocatalytic performance of nickel phosphide (Ni_2P) in HER. Samarium-doped Ni_2P is prepared via a two-step vapor–solid reaction method. The effects of samarium doping are comprehensively analyzed from various aspects by performing several physical and electrochemical characterization tests. Concisely, samarium doping remarkably improves the electrocatalytic properties of pure Ni_2P, suggesting samarium as a remarkable dopant for efficient HER.

Experimental methods

Materials

$NiSO_4.6H_2O$, $NaH_2PO_2.H_2O$, $Sm(NO_3)_3.6H_2O$ and NaOH (precursors with high purity were obtained from Sigma-Aldrich company and consumed as received.)

Synthesis of the developed electrocatalysts

In this study, samarium doping was performed at 3 percentages, including 1, 3, and 5%mol, and the corresponding samples were named $Sm_{0.01}Ni_2P$, $Sm_{0.03}Ni_2P$, and $Sm_{0.05}Ni_2P$, respectively. Sm-doped Ni_2P was synthesized by a two-step vapor–solid reaction (VSR) process. Sm-doped $Ni(OH)_2$ was initially prepared using a precipitation technique. Typically, 2.037 g of $NiSO_4.6H_2O$ and 0.101 g of $Sm(NO_3)_3.6H_2O$ were dissolved in 155 ml of distilled water to make a precursor solution. Next, 15 ml of 1.0 M NaOH solution, as the precipitant, was added gradually to the precursor solution. The resultant mixture was moved into a 230 ml Teflon-lined stainless steel autoclave and was maintained for 12 h at 110 °C. Then, Sm-doped $Ni(OH)_2$ precipitate was achieved, washed several times with distilled water, and dried naturally in air to result in Sm-doped $Ni(OH)_2$ powder. In the second step, Sm-doped Ni_2P was synthesized by phosphorizing Sm-doped $Ni(OH)_2$ using a VSR. Typically, Sm-doped $Ni(OH)_2$ powder and $NaH_2PO_2.H_2O$ with a molar ratio of 1:5 were heated in a furnace for 2 h at 350 °C. When the furnace reached room temperature, Sm-doped Ni_2P was collected. Pure Ni_2P was synthesized using a similar procedure without using the samarium precursor in the first step.

Preparation of electrodes

A titanium sheet measuring 20 mm × 10 mm × 1 mm was used as the substrate. Prior to electrode preparation, the substrate was cleaned by washing with water, polishing with sandpaper, and etching with a 6.0 M HCl solution to remove impurities from the surface. 10 mg of the electrocatalyst was added to the mixture consisting of 200 µl of distilled water, 750 µl of ethanol, and 50 µl of a 5% wt polyvinylidene fluoride (PVDF) binder solution in N-Methylpyrrolidone (NMP). The mixture was then sonicated for 30 min to ensure a homogeneous ink. The electrocatalyst ink was subsequently dropped onto the prepared Ti sheet and left to dry at room temperature.

Electrocatalyst characterization

X-ray diffraction (XRD) test was carried out to investigate the crystalline structure of electrocatalysts using an Inel EQUINOX 3000 X-ray diffractometer with Cu Kα radiation. Field emission scanning electron microscopy (FE-SEM) images were taken to consider the morphology of electrocatalysts by using a TESCAN Mira3 microscope equipped with an energy-dispersive X-ray spectrometer (EDS). X-ray photoelectron spectroscopy (XPS) was performed to analyze the surface chemical composition of samples using a Bestec EA10 plus spectrometer with aluminum radiation. The gas (nitrogen) sorption test was conducted to calculate electrocatalysts' specific surface area (SSA) using a Belsorp mini II surface area and pore size analyzer.

Electrochemical measurements

Electrochemical measurements were performed using an AUTOLAB potentiostat in a typical three-electrode cell. The synthesized electrocatalyst, Ag/AgCl electrode, and graphite rod were used as the working, reference, and

counter electrodes, respectively. All electrochemical measurements were carried out in 1.0 M KOH solution. The activity of electrocatalysts in HER was assessed by linear sweep voltammetry (LSV) with a scan rate of 5 mV/s. The recorded potentials were corrected by considering the corresponding potential drop of electrolyte resistance to monitor only the electrocatalysts' performance. Also, all potentials were converted to the reversible hydrogen electrode (RHE) using the following formula: E(RHE) = E(Ag/AgCl) + 0.199 + 0.059 × pH. The current densities were calculated relative to the geometric surface of electrodes under the electrolyte. The double-layer capacitance (C_{dl}) and electrochemical active surface area (ECSA) of electrocatalysts were obtained by conducting cyclic voltammetry (CV) at different scan rates from 10 to 100 mV/s in a potential window around open circuit potential (OCP) (OCP ± 0.1 V). The charge transfer behavior of electrocatalysts was considered by electrochemical impedance spectroscopy (EIS) in the frequency range from 0.1 Hz to 100 kHz. The stability of electrocatalysts was assessed by chronoamperometry at the overpotential in which the current density almost equaled 10 mA/cm^2.

Turnover frequency (TOF) calculation procedure

In the HER field, TOF is defined according to Eq. (1)[41].

$$TOF = \frac{number\ of\ produced\ hydrogen\ molecules\ per\ unit\ of\ time}{number\ of\ active\ sites} \tag{1}$$

The number of hydrogen molecules produced per second in HER, when the current density is reported based on the geometric surface of the electrocatalysts, can be calculated from Eq. (2):

$$N\left[\frac{molecule}{s}\right] = i\left[\frac{mA}{cm^2}\right] \times geometric\ surface\left[cm^2\right] \times 3.12 \times 10^{15}\left[\frac{molecule}{mAs}\right] \tag{2}$$

where N and i are the number of produced hydrogen molecules and current density, respectively, and 3.12×10^{15} molecule/mA s is a conversion factor. The number of active sites can be calculated by considering the electrochemical active surface area (ECSA) and the number of surface atoms per ECSA. To estimate the number of surface atoms per ECSA for Ni_2P, including both nickel and phosphorous as active sites, the unit cell of Ni_2P with a volume of 100.54 $\dot{A}^3$ is taken into account. This unit cell consists of 6 nickel atoms and 3 phosphorous atoms. Therefore, the number of surface atoms per ECSA is calculated by 2.00×10^{15} atom/cm^2. By substituting the obtained terms in formula 1, the TOF is calculated from Eq. 3:

$$TOF\left[\frac{molecule}{satom}\right] = \frac{i\left[\frac{mA}{cm^2}\right] \times geometric\ surface\left[cm^2\right] \times 3.12 \times 10^{15}\left[\frac{molecule}{mAs}\right]}{ECSA[cm^2] \times 2.00 \times 10^{15}[\frac{atom}{cm^2}]} \tag{3}$$

Results and discussion

The crystalline structure of materials was investigated by XRD test (Fig. 1a). The XRD pattern of pristine nickel hydroxide and Sm-doped nickel hydroxides correspond to the β-$Ni(OH)_2$ reference pattern (ICDD: 00-014-0117) without any peak related to Sm-based materials. The XRD pattern of pure and Sm-doped nickel phosphides corresponds well to the Ni_2P reference pattern (ICDD: 01-074-1385), and no unknown peaks attributed to Sm-containing compounds or impurities are detected. Close examination of XRD patterns reveals that the X-ray diffractogram of Sm-doped nickel phosphides has been negatively shifted to lower angles relative to the pure Ni_2P pattern. Figure 1b clearly depicts this peak shift around the characteristic pick of Ni_2P ((111) plane). As per Bragg's law, negative shift in XRD patterns stems from unit cell expansion[42]. Since samarium has a larger

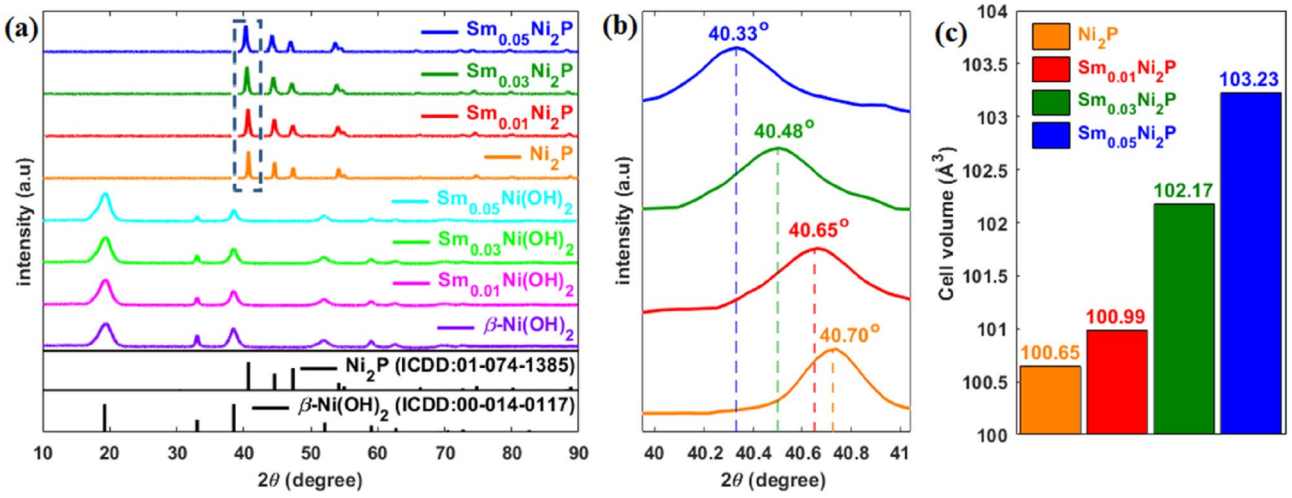

Figure 1. (**a**) XRD pattern of samples; (**b**) high-resolution XRD pattern of nickel phosphide samples around (111) plane of Ni_2P; (**c**) cell volume of nickel phosphide samples.

atomic radius than nickel, the unit cell expands accordingly when doped to Ni_2P and replaces the nickel in the structure[43]. This proposition was verified by calculating cell volume for different samples as illustrated in Fig. 1c. Sm-doped Ni_2P samples have larger cell volume than pure Ni_2P, and the cell volume increases as the doping level increases, which further confirms successful samarium doping and the proposed explanation for peak shift.

The morphology and particle size distribution of electrocatalysts were investigated using FE-SEM images. Figure 2a–f depicts FE-SEM images and the corresponding particle size distribution of pure Ni_2P and $Sm_{0.03}Ni_2P$. Both pure Ni_2P and $Sm_{0.03}Ni_2P$ samples exhibit pseudo-spherical agglomerated nanoparticles, and samarium has not noticeably changed the morphology. However, while samarium doping had a negligible effect on the morphology, it considerably affected the particle size. Based on the particle size distributions (Fig. 2c,f), the mean particle size of pure Ni_2P and $Sm_{0.03}Ni_2P$ was obtained at 136 and 36 nm, respectively, showing that samarium has significantly reduced the particle size. This effect also has been reflected in the SSA of samples. Figure 2g,h show the N_2 adsorption–desorption isotherms for pure Ni_2P and $Sm_{0.03}Ni_2P$, respectively. Based on International Union of Pure and Applied Chemistry (IUPAC) classifications, both isotherms are classified as type IV with a hysteresis of type H1 and H4 for pure Ni_2P and $Sm_{0.03}Ni_2P$, respectively, suggesting the samples possess mesoporous structure[44]. The pore size distribution of $Sm_{0.03}Ni_2P$ calculated by the Barrett–Joyner–Halenda (BJH) model with

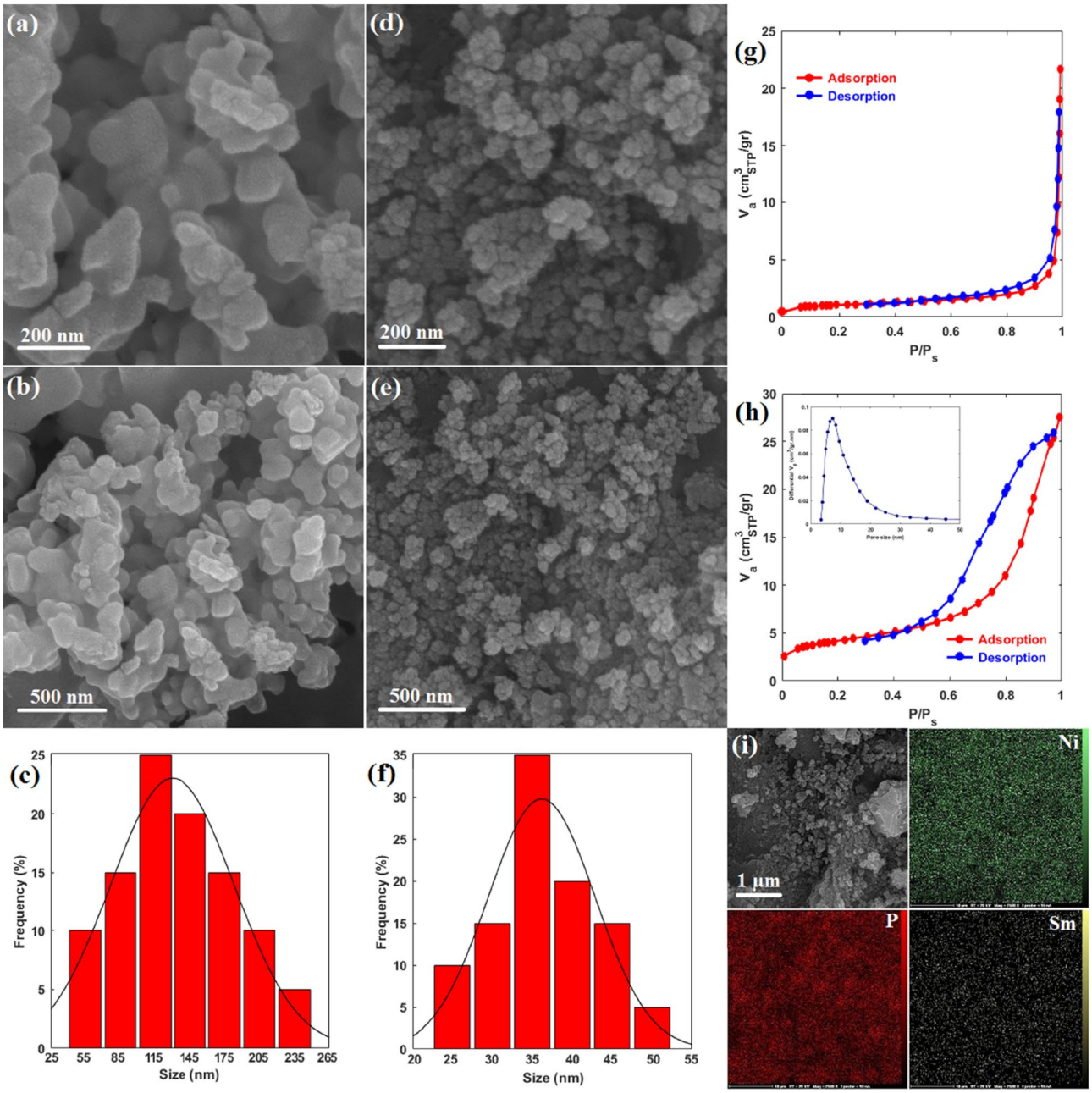

Figure 2. FE-SEM images and the respective particle size distribution of (**a**–**c**) Pure Ni_2P and (**d**–**f**) $Sm_{0.03}Ni_2P$; N_2 adsorption/desorption isotherms of (**g**) Pure Ni_2P (**h**) $Sm_{0.03}Ni_2P$; (**i**) SEM image and the respective elemental mapping of $Sm_{0.03}Ni_2P$.

diameters in the range of 2–50 nm clearly confirms the mesoporous structure (inset of Fig. 2h). Accordingly, the Brunauer–Emmett–Teller (BET) model[45] with an acceptable validity for mesoporous materials was used to calculate SSA. The SSA of pure Ni_2P and $Sm_{0.03}Ni_2P$ was calculated at 3.77 and 14.76 m^2/g respectively, which is consistent with the particle size analysis corroborating that samarium doping reduced the particle size. To discover the cause of this effect, the crystallite size of (111) crystalline plane of nickel phosphide samples was calculated using the Scherrer equation (Eq. 5)[46].

$$d = \frac{K\lambda}{WCos\theta} \tag{5}$$

D, K, λ, W, and θ represent average crystallite size, dimensionless shape factor, radiation wavelength (X-ray wavelength), full width at half maximum, and diffraction angle. The crystallite size of (111) plane for pure Ni_2P, $Sm_{0.01}Ni_2P$, $Sm_{0.03}Ni_2P$, and $Sm_{0.05}Ni_2P$ was obtained at 29.01, 28.90, 26.11, and 24.17 nm, respectively, clearly demonstrating that samarium incorporation has reduced the crystallite size. It is because when samarium atoms are doped into the structure of Ni_2P, they take the place initially held by nickel atoms. Since the atomic radius and valence of samarium and nickel considerably differ, the introduction of samarium makes the structure of Ni_2P less thermodynamically stable and results in reduced crystallite growth compared to the pure condition[47]. As a result, since crystallites constitute particles, a decrease in crystallite size leads to a corresponding decrease in particle size.

The surface composition and samarium doping amount were determined using EDS (Table 1). The atomic ratio of nickel to phosphorous (Ni:P) in all samples closely aligns with the respective 2:1 stoichiometric ratio in Ni_2P, corroborating the phase identification by XRD. Also, the atomic ratio of samarium to nickel (Sm:Ni) in the Sm-doped samples acceptably matches the respective nominal ratios, demonstrating precise samarium doping. The surface distribution of elements was studied using elemental mapping (Fig. 2i). The results show the existence of Ni, P, and Sm elements and their uniform distribution across the surface, which verifies successful samarium doping as well as the homogeneity of the sample.

The surface composition of $Sm_{0.03}Ni_2P$ was further analyzed using XPS, as illustrated in Fig. 3. The general survey spectrum (Fig. 3a) reveals distinct peaks related to the energy levels of P, Ni, and Sm elements, indicating their presence on the surface. The high-resolution P 2p energy level spectrum (Fig. 3b) shows two peaks at 129.4 and 128.5 eV, corresponding to P $2p_{1/2}$ and P $2p_{3/2}$ energy levels, respectively. Additionally, a peak at 133.2 eV is observed, indicating the presence of oxidized P species.[48]. P 2p energy level peaks have shifted to lower binding energies relative to their normal positions (130.0 eV), indicating that the phosphorous atoms have been partially negatively charged. This shift provides evidence of electron sharing between the nickel and phosphorous atoms, supporting the formation of nickel phosphide compounds[49]. The high-resolution Ni 2p energy level spectrum (Fig. 3c) displays two peaks at 874.5 and 856.6 eV, corresponding to the Ni $2p_{1/2}$ and Ni $2p_{3/2}$ energy levels, respectively. Two additional 879.7 eV and 861.4 peaks are assigned to satellites of the corresponding energy levels[50]. The high-resolution Sm 3d energy level spectrum (Fig. 3d) depicts two peaks at 1083.0 and 1109.8 eV, which match Sm $3d_{5/3}$ and $3d_{3/2}$ energy levels, respectively. The latter photoelectron lines, which correspond to Sm (III), further confirm the successful doping of samarium[51].

The activity of electrocatalysts toward HER was assessed by LSV in a 1.0 M KOH solution at room temperature (Fig. 4a). The bare Ti sheet substrate exhibits negligible activity, indicating that the performance of the electrocatalysts almost entirely stems from the loaded active materials. As observed, samarium can improve the activity of pure Ni_2P with an optimum doping level of 3%mol. Figure 4b depicts the overpotentials at different current densities for other electrocatalysts. $Sm_{0.03}Ni_2P$ with overpotentials of 130.6 and 198.5 mV at current densities of 10 and 100 mA/cm^2 shows the highest electrocatalytic activity toward HER and $Sm_{0.01}Ni_2P$, $Sm_{0.05}Ni_2P$, and pure Ni_2P follow in the subsequent rank, respectively.

The kinetics of HER were analyzed using the Tafel plot (Fig. 4c). Ni_2P with a Tafel slope of 152.3 mV/dec. suggests that it electrocatalyzes the HER via a controlling Volmer reaction, meaning that it suffers from immoderate electrochemical hydrogen adsorption[52]. However, samarium doping has reduced the Tafel slope of pristine Ni_2P to values that allow the HER to proceed through the Volmer–Heyrovsky mechanism with a fast Volmer reaction and a controlling Heyrovsky reaction, which signifies that samarium doping has moderated the electrochemical hydrogen adsorption[53]. This is most significant at 3%mol of samarium doping, where $Sm_{0.03}Ni_2P$ exhibited the lowest Tafel slope of 67.8 mV/dec., indicating that its highest activity partly originates from its moderate electrochemical hydrogen adsorption. The kinetics of HER was further investigated by analyzing the charge transfer coefficient. The charge transfer coefficient represents the fraction of the interfacial potential used to overcome the energy barriers of an electrochemical reaction and, therefore, can be considered an illustrating indicator of energy efficiency. Figure 4d depicts the charge transfer coefficient of electrocatalysts. Pure Ni_2P with the lowest charge transfer coefficient demonstrates comparatively poor energy efficiency. However, samarium doping

Sample	Ni (%at)	P (%at)	Sm (%at)	Ni:P	Sm:Ni
Ni_2P	66.2	33.8	–	1.96	–
$Sm_{0.01}Ni_2P$	65.3	34.1	0.6	1.91	0.009
$Sm_{0.03}Ni_2P$	64.4	33.9	1.7	1.9	0.026
$Sm_{0.05}Ni_2P$	63.2	34.0	2.8	1.86	0.044

Table 1. Surface composition by EDS for different samples.

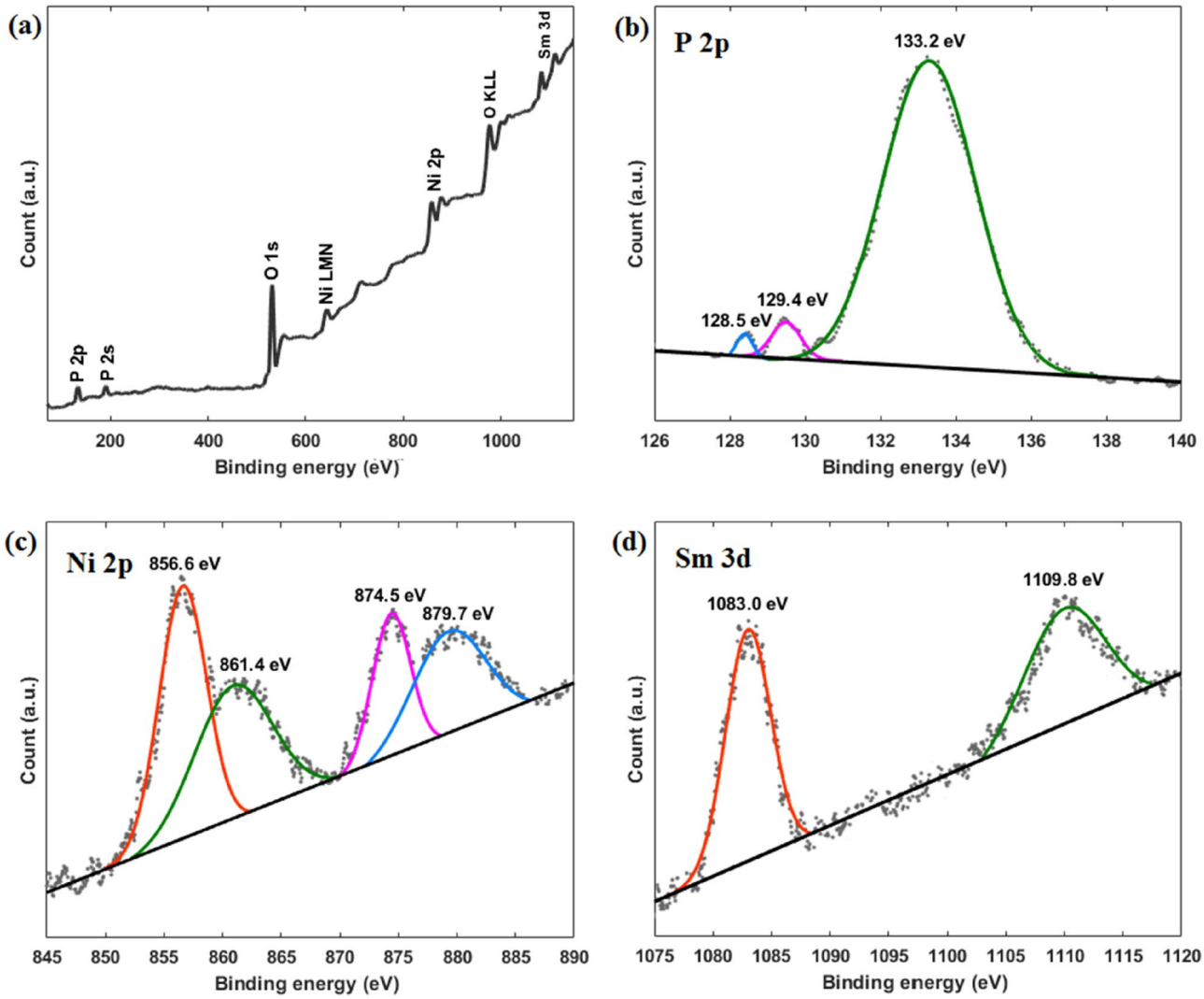

Figure 3. XPS spectrum of $Sm_{0.03}Ni_2P$ in different regions: (**a**) general survey. (**b**) P 2p. (**c**) Ni 2p. (**d**) Sm 3d.

improved the energy efficiency, and Sm-doped Ni_2P electrocatalysts generally exhibit higher charge transfer coefficients than pure Ni_2P. Also, $Sm_{0.03}Ni_2P$ possesses the highest charge transfer coefficient, contributing to its better electrocatalytic performance.

The electrochemical active surface area (ECSA) of electrocatalysts was analyzed using the electrochemical double-layer capacitance calculated from the CV test. Figure 5a–d shows the CV curves of different electrocatalysts. The difference between non-faradic currents in anodic and cathodic paths was extracted and plotted against scan rate as shown in Fig. 5e, in which half of the slope indicates the double layer capacitance. As the electrochemical double-layer capacitance and ECSA are linearly proportional to each other, the ECSA was obtained by assuming a specific capacitance of 40 $\mu F/cm^2$ per 1 cm^2 of ECSA for an electrocatalyst with a smooth surface (Fig. 5f)[54–56]. The surface of pure Ni_2P exhibits a relatively weak activity toward HER. However, samarium doping has considerably activated the pure Ni_2P surface. Also, $Sm_{0.03}Ni_2P$ has exposed the largest ECSA, and its highest activity can be related to some extent to its more electrochemically active surface. Given the different SSA of pure Ni_2P and $Sm_{0.03}Ni_2P$, to clarify whether the higher activity of $Sm_{0.03}Ni_2P$ solely stems from its larger SSA, the LSV curves were normalized concerning SSA. As shown in Fig. 5g., $Sm_{0.03}Ni_2P$ even after eliminating the effect of SSA demonstrates a higher activity, indicating that samarium doping not only has increased the surface area but also more significantly has activated a previously inactive surface toward HER electrocatalysis.

The effect of samarium doping on the electrocatalytic strength and intrinsic activity of active sites was analyzed using the turnover frequency (TOF) parameter. In the field of HER, TOF is defined as the number of H_2 molecules an active site generates per unit of time, providing a helpful measure of the electrocatalyst's intrinsic activity. Figure 5h exhibits the TOF curve of different samples. Samarium doping increases the TOF and, consequently, the intrinsic activity of pure Ni_2P. Namely, Fig. 5i illustrates the needed overpotential of different samples at TOF of 100 $\frac{1}{s}$, where $Sm_{0.01}Ni_2P$, $Sm_{0.03}Ni_2P$, and $Sm_{0.05}Ni_2P$ with overpotentials of 306.2, 296.5, 349.4 mV respectively, require lower overpotential than pure Ni_2P (420.6 mV) and exhibit greater intrinsic activity. LSV curves normalized with respect to ECSA further illustrate this effect, as Sm-doped electrocatalysts have shown better performance compared to pure Ni_2P (Fig. 5j). It is worth mentioning that $Sm_{0.03}Ni_2P$ showed the

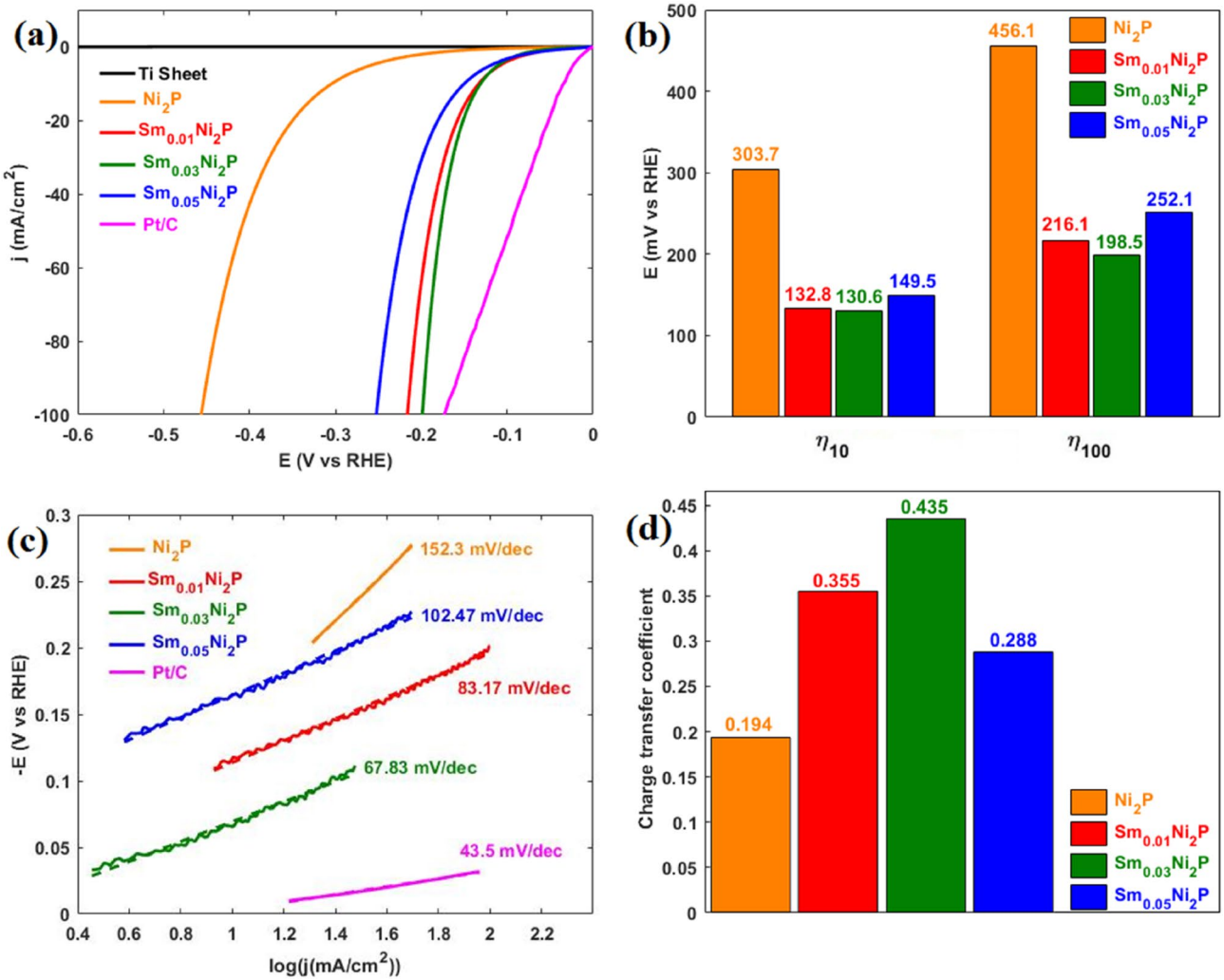

Figure 4. (**a**) LSV curve of electrocatalysts in 1.0 M KOH; (**b**) overpotentials of electrocatalysts at current densities of 10 and 100 $\frac{mA}{cm^2}$; (**c**) corresponding Tafel plot of electrocatalysts; (**d**) charge transfer coefficient of electrocatalysts.

highest TOF, particularly at high overpotentials, and as such, its superior performance could be attributed to its intrinsically more robust active sites.

The electrocatalyst-electrolyte interface properties in the electrochemical cell were investigated using electrochemical impedance spectroscopy. Figure 5k exhibits the Nyquist plot of different samples. Pure Ni_2P, with the largest semi-circle diameter, shows the highest charge transfer resistance. However, samarium doping improved the charge transfer behavior of pure Ni_2P, as evidenced by the smaller semi-circle diameters and, consequently, lower charge transfer resistances of the Sm-doped Ni_2P electrocatalysts compared to pure Ni_2P[57]. The smallest semi-circle diameter was observed for the $Sm_{0.03}Ni_2P$ electrocatalyst, suggesting that its superior activity can be ascribed to a degree to its optimized charge transfer ability. Nyquist plots were further analyzed by defining an appropriate Randles equivalent circuit (see inset of Fig. 5k) for the electrochemical system to provide a quantitative insight into the electrocatalyst-electrolyte interface. Figure 5l illustrates the charge transfer resistance (R_{ct}) of electrocatalysts, where consistent with the qualitative analysis, samarium doping decreases the (R_{ct}) of pure Ni_2P by more than 80%, and the lowest charge transfer resistance can be observed by $Sm_{0.03}Ni_2P$.

The stability and durability of $Sm_{0.03}Ni_2P$ as the best electrocatalyst of the present study were investigated by chronoamperometry to assess its practical application suitability[58]. Figure 6a shows the chronoamperometry for $Sm_{0.03}Ni_2P$ at an overpotential of 0.15 V (vs. RHE), where the steady current density-time plot with less than 5% decrease in activity after 24 h indicates the stable performance of the electrocatalyst. Figure 6b compares the LSV curves of $Sm_{0.03}Ni_2P$ before and after the stability test, where the negligible difference between two activity trends implies the durable performance of the electrocatalyst, suggesting $Sm_{0.03}Ni_2P$ as a high-potential material for real electrochemical applications. The used sample was then characterized after the stability test. Figure 6c compares the XRD patterns of the used electrocatalyst before and after the stability test, revealing no phase change and noticeable alteration in crystalline structure. Figure 6d,e display the SEM images of the used and fresh electrocatalysts, respectively, demonstrating that the morphology and size of the particles have remained almost intact. Consequently, these results further support the notion of the electrocatalyst's stable and durable

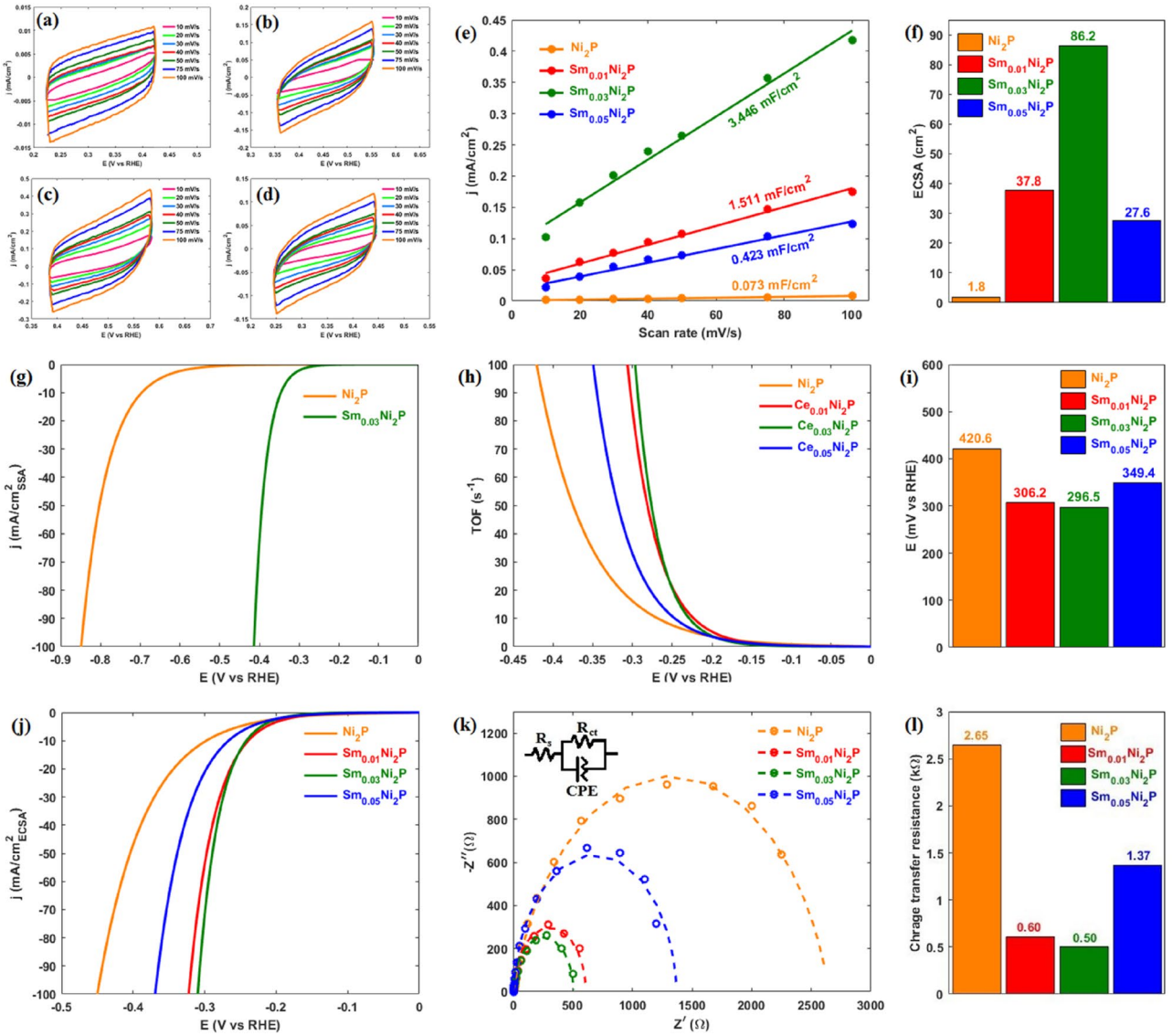

Figure 5. CV curves of electrocatalysts: (**a**) Ni_2P (**b**) $Sm_{0.01}Ni_2P$ (**c**) $Sm_{0.03}Ni_2P$ (**d**) $Sm_{0.05}Ni_2P$; (**e**) Capacitive current density vs. scan rate of electrocatalysts; (**f**) ECSA of electrocatalysts; (**g**) LSV curve of Ni_2P and $Sm_{0.03}Ni_2P$ in 1.0 M KOH normalized to SSA; (**h**) TOF curve of electrocatalysts; (**i**) Overpotential of electrocatalysts at TOF of 100 $\frac{1}{s}$; (**j**) LSV curve of electrocatalysts in 1.0 M KOH normalized to ECSA; (**k**) Nyquist plot of electrocatalysts; (**l**) charge transfer resistance of electrocatalysts.

performance, as well as its robust structure. Finally, the Farady efficiency of $Sm_{0.03}Ni_2P$ was calculated by measuring the amount of evolved H_2 at a constant current density of 10 mA/cm^2 at 10-min intervals for 1 h. Figure 6f shows the actual and theoretical amount of hydrogen evolution, where the proximity of these two values leads to Faraday efficiency of nearly 100%, highlighting the exceptional performance of the electrocatalyst.

$Sm_{0.03}Ni_2P$ electrocatalyst, by demonstrating considerable performance in HER, proved to be the best electrocatalyst of this study. Table 2 compares its performance with recent studies that employed transition metal-based materials in alkaline HER. $Sm_{0.03}Ni_2P$ outperformed other electrocatalysts in this study and outclassed multiple other electrocatalysts, highlighting its potential as a promising electrocatalyst for efficient HER.

Conclusion

In this study, samarium doping was presented as an innovative approach to improve the electrocatalytic performance of Ni_2P in HER. Samarium doping was carried out at different levels of 1, 3, and 5%mol to comprehensively investigate its effects on the characteristics of pure Ni_2P. Physical characterization tests demonstrated that samarium doping decreased the particle size of pure Ni_2P as a result of crystallite growth inhibition and consequently increased the SSA. Electrochemical analyses showed that samarium doping increased the electrocatalytic activity of pure Ni_2P in HER by modifying the electrochemical hydrogen adsorption, intrinsic activity, SSA, ECSA, and charge transfer behavior. The optimum level of samarium doping was found at 3%mol, where

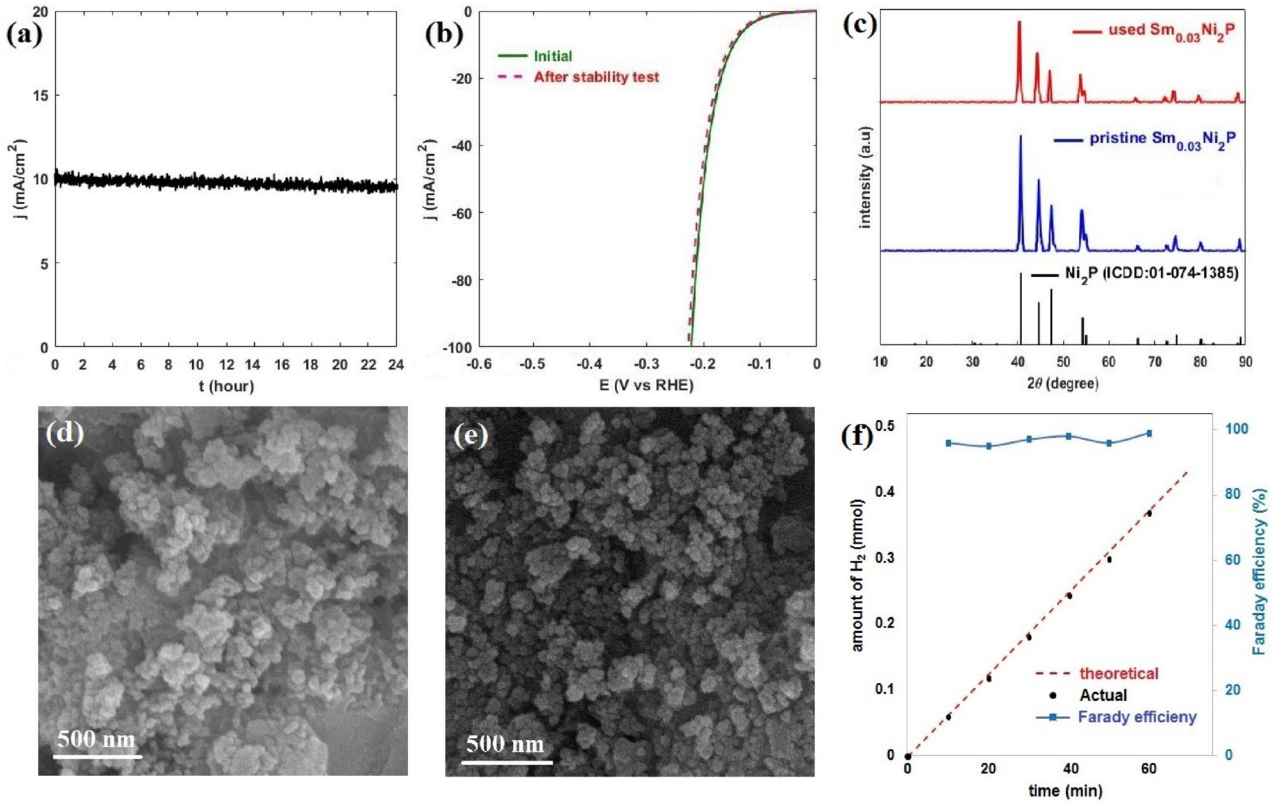

Figure 6. (**a**) Chronoamperometry test of $Sm_{0.03}Ni_2P$; (**b**) LSV curves of $Sm_{0.03}Ni_2P$ before and after stability test; (**c**) XRD pattern of pristine and used $Sm_{0.03}Ni_2P$; (**d**) SEM image of used $Sm_{0.03}Ni_2P$; (**e**) SEM image of fresh $Sm_{0.03}Ni_2P$; (**f**) Faraday efficiency and amount of actual and theoretical H_2 evolution of $Sm_{0.03}Ni_2P$.

Electrocatalyst	η_{10}(mV vs. RHE)	b ($\frac{mV}{dec.}$)	References
$Sm_{0.03}Ni_2P$	130.6	67.8	Present study
Ce-doped Ni_2P	158	95.6	[38]
La-doped Ni_2P	226	126.7	[38]
Ce-doped CoMoP/MoP@C	188	72.2	[59]
Ni_5P4-NiP_2-Ni_2P/NC	202	74	[60]
Ni-doped $MoSe_2$	206	81	[61]
Co-doped $MoSe_2$	212	99	[61]
Co-doped1T-MoS_2	240	68	[62]
NiFeP@C	160	78.5	[63]
$FeCoP_2$@NPPC	150	79	[64]
NiMoP	400	163	[65]
CoP-CoTe2	178	112	[66]
Ce-doped Ni_2P	150	76.8	[41]
F-doped carbon dot/CoP	16	89	[67]
N-doped Ni_2P	110	108	[68]

Table 2. Comparison of the present research with recent studies in alkaline HER.

$Sm_{0.03}Ni_2P$, thanks to its optimized properties, showed a remarkable performance in HER, which introduces samarium and $Sm_{0.03}Ni_2P$ as capable dopant and efficient electrocatalysts for HER, respectively.

Data availability

The data that support the findings of this study are available from the corresponding author upon reasonable request.

Received: 4 March 2024; Accepted: 3 July 2024
Published online: 22 July 2024

References

1. Golrokhifar, S., Shahroudi, A. & Habibzadeh, S. Cost-effective electrodeposited mixed transition metal electrocatalysts for efficient hydrogen evolution reaction. *Electrocatalysis* 1–8 (2024).
2. Gong, Y., Xu, L. H., Li, J. & Shan, D. Confinement of transition metal phosphides in N, P-doped electrospun carbon fibers for enhanced electrocatalytic hydrogen evolution. *J. Alloys Compd.* **875**, 159934 (2021).
3. Pu, Z. *et al.* Versatile route to fabricate precious-metal phosphide electrocatalyst for acid-stable hydrogen oxidation and evolution reactions. *ACS Appl. Energy Mater.* **12**, 11737–11744 (2020).
4. Zhang, G. *et al.* Highly active and stable catalysts of phytic acid-derivative transition metal phosphides for full water splitting. *J. Am. Chem. Soc.* **138**, 14686–14693 (2016).
5. Shahroudi, A., Esfandiari, M. & Habibzadeh, S. Nickel sulfide and phosphide electrocatalysts for hydrogen evolution reaction: challenges and future perspectives. *RSC Adv.* **12**, 29440–29468 (2022).
6. Pu, Z. *et al.* Transition-metal phosphides: activity origin, energy-related electrocatalysis applications, and synthetic strategies. *Adv. Funct. Mater.* **30**, 2004009 (2020).
7. Jin, Y. *et al.* Preparation of mesoporous Ni2P nanobelts with high performance for electrocatalytic hydrogen evolution and supercapacitor. *Int. J. Hydrog. Energy* **43**, 3697–3704 (2018).
8. Yan, Q. *et al.* Hierarchical edge-rich nickel phosphide nanosheet arrays as efficient electrocatalysts toward hydrogen evolution in both alkaline and acidic conditions. *ACS Sustain. Chem. Eng.* **7**, 7804–7811 (2019).
9. Yu, X. *et al.* "Superaerophobic" nickel phosphide nanoarray catalyst for efficient hydrogen evolution at ultrahigh current densities. *J. Am. Chem. Soc.* **141**, 7537–7543 (2019).
10. Wu, X. *et al.* Plasma enabled non-thermal phosphorization for nickel phosphide hydrogen evolution catalysts. *Chem. Commun.* **55**, 4202–4205 (2019).
11. Pu, Z. *et al.* Phytic acid-derivative transition metal phosphides encapsulated in N, P-codoped carbon: an efficient and durable hydrogen evolution electrocatalyst in a wide pH range. *Nanoscale* **9**, 3555–3560 (2017).
12. Gao, W. K. *et al.* In situ construction of surface defects of carbon-doped ternary cobalt-nickel-iron phosphide nanocubes for efficient overall water splitting. *SCMs* **9**, 1285–1296 (2019).
13. Lu, S. S. *et al.* Tungsten-doped Ni–Co phosphides with multiple catalytic sites as efficient electrocatalysts for overall water splitting. *J. Mater. Chem. A* **7**, 16859–16866 (2019).
14. Esfandiari, M., Habibzadeh, S. & Halladj, R. Efficient hierarchical ZIF-based electro/photocatalyst toward hydrogen generation and evolution. *Int. J. Hydrog. Energy* **64**, 806–818 (2024).
15. Liu, W. *et al.* Ferrum-molybdenum dual incorporated cobalt oxides as efficient bifunctional anti-corrosion electrocatalyst for seawater splitting. *Appl. Catal. B* **328**, 122488 (2023).
16. Li, K., Tong, Y., He, J., Liu, X. Y. & Chen, P. Anion-modulated CoP electrode as bifunctional electrocatalyst for anion-exchange membrane hydrazine-assisted water electrolyser. *Mater. Horiz.* **10**, 5277–5287 (2023).
17. Li, K., Zhou, G., Tong, Y., Ye, Y. & Chen, P. Interface engineering of a hierarchical p-modified Co/Ni3P heterostructure for highly efficient water electrolysis coupled with hydrazine degradation. *ACS Sustain. Chem. Eng.* **11**, 14186–14196 (2023).
18. Li, K., He, J., Guan, X., Tong, Y., Ye, Y., Chen, L. & Chen, P. Phosphorus-modified amorphous high-entropy CoFeNiCrMn compound as high-performance electrocatalyst for hydrazine-assisted water electrolysis. *Small* 2302130 (2023).
19. Feng, D., Liu, X. Y., Ye, R., Huang, W. & Tong, Y. Carbon-encapsulated Co2P/P-modified NiMoO4 hierarchical heterojunction as superior pH-universal electrocatalyst for hydrogen production. *J. Colloid Interface Sci.* **634**, 693–702 (2023).
20. Feng, D., Ren, X. & Tong, Y. Rational design of tungsten-doped cobalt molybdate nanosheet arrays for highly active ethanol-assisted hydrogen production. *Int. J. Hydrog. Energy* (2023).
21. Damhus, T., Hartshorn, R.M. & Hutton, A.T. Nomenclature of inorganic chemistry: IUPAC recommendations. *Chem. Int.* (2005).
22. Yaroshevsky, A. A. Abundances of chemical elements in the Earth's crust. *Geochem. Int.* **44**, 48–55 (2006).
23. Haxel, G. *Rare earth elements: critical resources for high technology* (Vol. 87, No. 2). US Department of the Interior, US Geological Survey (2002).
24. Huang, H. & Zhu, J. J. The electrochemical applications of rare earth-based nanomaterials. *Anlst* **144**, 6789–6811 (2019).
25. Gao, W., Wen, D., Ho, J. C. & Qu, Y. Incorporation of rare earth elements with transition metal–based materials for electrocatalysis: A review for recent progress. *Mater. Today Chem.* **12**, 266–281 (2019).
26. Gao, W. *et al.* Modulating electronic structure of CoP electrocatalysts towards enhanced hydrogen evolution by Ce chemical doping in both acidic and basic media. *Nano Energy* **38**, 290–296 (2017).
27. Li, J., Zou, S., Liu, X., Lu, Y. & Dong, D. Electronically modulated CoP by Ce doping as a highly efficient electrocatalyst for water splitting. *ACS Sustain. Chem. Eng.* **8**, 10009–10016 (2020).
28. Chen, T. *et al.* Ce-doped CoP nanoparticles embedded in carbon nanotubes as an efficient and durable catalyst for hydrogen evolution. *Nanotechnology* **31**, 125402 (2020).
29. Liu, P. *et al.* Cerium and nitrogen doped CoP nanorod arrays for hydrogen evolution in all pH conditions. *Sustain. Energy Fuels* **3**, 3344–3351 (2019).
30. Zhang, G., Wang, B., Bi, J., Fang, D. & Yang, S. Constructing ultrathin CoP nanomeshes by Er-doping for highly efficient bifunctional electrocatalysts for overall water splitting. *J. Mater. Chem. A* **7**, 5769–5778 (2019).
31. Morse, S. L. & Greene, N. D. Hydrogen overpotential on rare earth metals. *Electrochim. Acta* **12**, 179–189 (1967).
32. Van Vucht, J. H., Kuijpers, F. & Bruning, H. C. Reversible room-temperature absorption of large quantities of hydrogen by intermetallic compounds. *Philips Res. Rep* **25**, 133–140 (1970).
33. Miles, M. H. Evaluation of electrocatalysts for water electrolysis in alkaline solutions. *J. Electroanal. Chem. Interfacial Electrochem.* **60**, 89–96 (1975).
34. Kitamura, T., Iwakura, C. & Tamura, H. Hydrogen evolution at LaNi5 and MmNi5 electrodes in alkaline solutions. *Chem. Lett.* **10**, 965–966 (1981).
35. Dominguez-Crespo, M. A., Torres-Huerta, A. M., Brachetti-Sibaja, B. & Flores-Vela, A. Electrochemical performance of Ni–RE (RE= rare earth) as electrode material for hydrogen evolution reaction in alkaline medium. *Int. J. Hydrog. Energy* **36**, 135–151 (2011).
36. Santos, D. M. F. *et al.* Electrocatalytic activity of nickel-cerium alloys for hydrogen evolution in alkaline water electrolysis. *J. Electrochem. Soc.* **161**, 386 (2014).
37. Rosalbino, F., Macciò, D., Saccone, A., Angelini, E. & Delfino, S. Fe–Mo–R (R= rare earth metal) crystalline alloys as a cathode material for hydrogen evolution reaction in alkaline solution. *Int. J. Hydrog. Energy* **36**, 1965–1973 (2011).
38. Wang, Q. *et al.* RE-doped (RE= La, Ce and Er) Ni 2 P porous nanostructures as promising electrocatalysts for hydrogen evolution reaction. *Dalton Trans.* **52**, 1895–1901 (2023).
39. Xiong, K. *et al.* Cerium-incorporated Ni2P nanosheets for enhancing hydrogen production from overall water splitting and urea electrolysis. *J. Alloys Compd.* **912**, 165234 (2022).

40. Zhang, H. *et al.* Cerium-doped nickel phosphide nanosheet arrays as highly efficient electrocatalysts for the hydrogen evolution reaction in acidic and alkaline conditions. *ACS Appl. Energy Mater.* **5**, 10961–10972 (2022).
41. Shahroudi, A., Keivanimehr, F. & Habibzadeh, S. Cerium-doped nickel phosphide (Ni2P): Highly efficient electrocatalyst for hydrogen evolution reaction. *Int. J. Hydrog. Energy* **48**, 39885–39899 (2023).
42. Bragg, W.H. & Bragg, W.L. The reflection of X-rays by crystals. *Proc. R. Soc. Lond. Ser. A Contain. Papers Math. Phys. Char.* **88**, 428–438 (1913).
43. Clementi, E. & Raimondi, D. L. Atomic screening constants from SCF functions. *J. Chem. Phys.* **38**, 2686–2689 (1963).
44. Shahroudi, A. & Vahidi, O. Large-scale precipitation synthesis of α-alumina with poly aluminum chloride: Optimization of synthesis parameters. *Int. J. Appl. Ceram.* **20**, 1526–1534 (2023).
45. Brunauer, S., Emmett, P. H. & Teller, E. Adsorption of gases in multimolecular layers. *J. Am. Chem. Soc.* **60**, 309–319 (1938).
46. Norouzbeigi, R. & Edrissi, M. Preparation of nano alumina powder via combustion synthesis: Porous structure optimization via Taguchi L16 design. *J. Am. Ceram. Soc.* **94**, 4052–4058 (2011).
47. Huang, H. *et al.* Iron-tuned super nickel phosphide microstructures with high activity for electrochemical overall water splitting. *Nano Energy* **34**, 472–480 (2017).
48. Huo, J. *et al.* Bifunctional iron nickel phosphide nanocatalysts supported on porous carbon for highly efficient overall water splitting. *SM&T* **22**, 00117 (2019).
49. Zheng, H. *et al.* Cobalt-tuned nickel phosphide nanoparticles for highly efficient electrocatalysis. *Appl. Surf. Sci.* **479**, 1254–1261 (2019).
50. Ren, Q. *et al.* Hydrogen evolution reaction catalyzed by nickel/nickel phosphide nanospheres synthesized through electrochemical methods. *Electrochim. Acta* **298**, 229–236 (2019).
51. Ramana, E. V. *et al.* Effect of samarium and vanadium co-doping on structure, ferroelectric and photocatalytic properties of bismuth titanate. *RSC Adv.* **7**, 9680–9692 (2017).
52. Pan, Y., Hu, W., Liu, D., Liu, Y. & Liu, C. Carbon nanotubes decorated with nickel phosphide nanoparticles as efficient nanohybrid electrocatalysts for the hydrogen evolution reaction. *J. Mater. Chem. A* **3**, 13087–13094 (2015).
53. Wang, X., Kolen'ko, Y. V., Bao, X. Q., Kovnir, K. & Liu, L. One-step synthesis of self-supported nickel phosphide nanosheet array cathodes for efficient electrocatalytic hydrogen generation. *Angew. Chem.* **127**, 8306–8310 (2015).
54. Dinh, K. N. *et al.* O2 plasma and cation tuned nickel phosphide nanosheets for highly efficient overall water splitting. *Nano Energy* **54**, 82–90 (2018).
55. Ledendecker, M., Schlott, H., Antonietti, M., Meyer, B. & Shalom, M. Experimental and theoretical assessment of ni-based binary compounds for the hydrogen evolution reaction. *Adv. Energy Mater.* **7**, 1601735 (2017).
56. Kumar, P. *et al.* Carbon supported nickel phosphide as efficient electrocatalyst for hydrogen and oxygen evolution reactions. *Int. J. Hydrog. Energy* **46**, 622–632 (2021).
57. Wang, J., Xu, F., Jin, H., Chen, Y. & Wang, Y. Non-noble metal-based carbon composites in hydrogen evolution reaction: Fundamentals to applications. *Adv. Mater.* **29**, 1605838 (2017).
58. Hosseinzadeh, N., Habibzadeh, S. & Halladj, R. A novel ternary Ti-V-Bi oxide photoelectrocatalyst in advanced oxidation process. *J. Alloys Compd.* **960**, 171064 (2023).
59. Chen, T. *et al.* Fabrication of cerium-doped CoMoP/MoP@ C heterogeneous nanorods with high performance for overall water splitting. *Energy Fuels* **35**, 14169–14176 (2021).
60. Pei, M. *et al.* Ni5P4-NiP2-Ni2P nanocomposites tangled with N-doped carbon for enhanced electrochemical hydrogen evolution in acidic and alkaline solutions. *Catal.* **12**, 1650 (2022).
61. Zhao, G. *et al.* Heteroatom-doped MoSe2 nanosheets with enhanced hydrogen evolution kinetics for alkaline water splitting. *Chem. Asian J.* **14**, 301–306 (2019).
62. Ma, F. *et al.* One-step synthesis of Co-doped 1T-MoS2 nanosheets with efficient and stable HER activity in alkaline solutions. *Mater. Chem. Phys.* **244**, 122642 (2020).
63. Kang, Q., Li, M., Shi, J., Lu, Q. & Gao, F. A universal strategy for carbon-supported transition metal phosphides as high-performance bifunctional electrocatalysts towards efficient overall water splitting. *ACS Appl. Mater. Interfaces* **12**, 19447–19456 (2020).
64. Wang, Y. N. *et al.* FeCoP2 nanoparticles embedded in N and P Co-doped hierarchically porous carbon for efficient electrocatalytic water splitting. *ACS Appl. Mater. Interfaces* **13**, 8832–8843 (2021).
65. Man, H. W. *et al.* Transition metal-doped nickel phosphide nanoparticles as electro-and photocatalysts for hydrogen generation reactions. *Appl. Catal. B* **242**, 186–193 (2019).
66. Amorim, I. *et al.* Dual-phase CoP–CoTe2 nanowires as an efficient bifunctional electrocatalyst for bipolar membrane-assisted acid-alkaline water splitting. *J. Chem. Eng.* **420**, 130454 (2021).
67. Song, H., Yu, J., Tang, Z., Yang, B. & Lu, S. Halogen-doped carbon dots on amorphous cobalt phosphide as robust electrocatalysts for overall water splitting. *Adv. Energy Mater.* **12**, 2102573 (2022).
68. Liu, K., Ma, Z., Li, J. & Wang, X. Theoretical expectation and experimental investigation on the feasibility of N-doped Ni2P as highly active hydrogen evolution catalyst. *Int. J. Hydrog. Energy* **51**, 713–724 (2023).

Author contributions

Ali Shahroudi: conceptualization, data curation, formal analysis, investigation, methodology, visualization, writing original draft, writing review and editing. Sajjad Habibzadeh: conceptualization, project administration, resources, supervision, writing original draft, writing review and editing.

Competing interests

The authors declare no competing interests.

Additional information

Correspondence and requests for materials should be addressed to S.H.

Reprints and permissions information is available at www.nature.com/reprints.

Publisher's note Springer Nature remains neutral with regard to jurisdictional claims in published maps and institutional affiliations.